Influence of strain-rate on the response of elastomeric architected materials

MacNider, Brianna C
Dattelbaum, Dana Mcgraw
Boechler, Nicholas
Cady, Carl Mcelhinney
Derby, Benjamin Kyle
Fensin, Saryu Jindal
Lee, Kwan-Soo
Kim, Jihyeon
Nakarmi, Sushan
Daphalapurkar, Nitin Pandurang

To be published in: Extreme Mechanics Letters

DOI to publisher's version: 10.1016/j.eml.2025.102389

Influence of strain-rate on the response of elastomeric architected materials

Brianna MacNider, Dana M. Dattelbaum, Nicholas Boechler, Carl Cady, Benjamin K. Derby, Saryu Fensin, Kwan-Soo Lee, Jihyeon Kim, Sushan Nakarmi, Nitin Daphalapurkar

PII: S2352-4316(25)00101-4

DOI: https://doi.org/10.1016/j.eml.2025.102389

Reference: EML102389

To appear in: *Extreme Mechanics Letters*

Received date: 3 February 2025
Revised date: 7 July 2025
Accepted date: 14 July 2025

Please cite this article as: Brianna MacNider, Dana M. Dattelbaum, Nicholas Boechler, Carl Cady, Benjamin K. Derby, Saryu Fensin, Kwan-Soo Lee, Jihyeon Kim, Sushan Nakarmi and Nitin Daphalapurkar, Influence of strain-rate on the response of elastomeric architected materials, *Extreme Mechanics Letters,* (2025) doi:https://doi.org/10.1016/j.eml.2025.102389

Influence of strain-rate on the response of elastomeric architected materials

Brianna MacNider[‡†*], Dana M. Dattelbaum[†*], Nicholas Boechler[‡], Carl Cady[†], Benjamin K. Derby[†], Saryu Fensin[†], Kwan-Soo Lee[†], Jihyeon Kim[†], Sushan Nakarmi[†],Nitin Daphalapurkar[†]

[†]Los Alamos National Laboratory, Los Alamos, NM 87545
[‡]University of California San Diego, La Jolla, CA 92093

*Corresponding author: danadat@lanl.gov

Abstract

Architected materials have shown substantial promise in impact mitigation and protective applications, and there has accordingly been great interest in better characterizing their response at elevated strain rates due to impact. There remains ambiguity regarding the contribution of inertial and material responses to strain rate sensitivity, and, in particular, when these effects begin to gain dominance in the impact response of an architected material. The response of soft polymer architected materials as a function of strain rate, in particular, has been little investigated. We characterize the experimental impact response of four soft polymer architected lattice geometries across varying strain rates in the intermediate strain rate regime (~10^3 s^{-1}) using split-Hopkinson pressure bar loading and high speed video characterization of the resulting deformation fields. Our results highlight the interplay of influence between constituent material, lattice geometry, length scale, and strain rate in determining the onset of significant inertia effects.

Graphical abstract

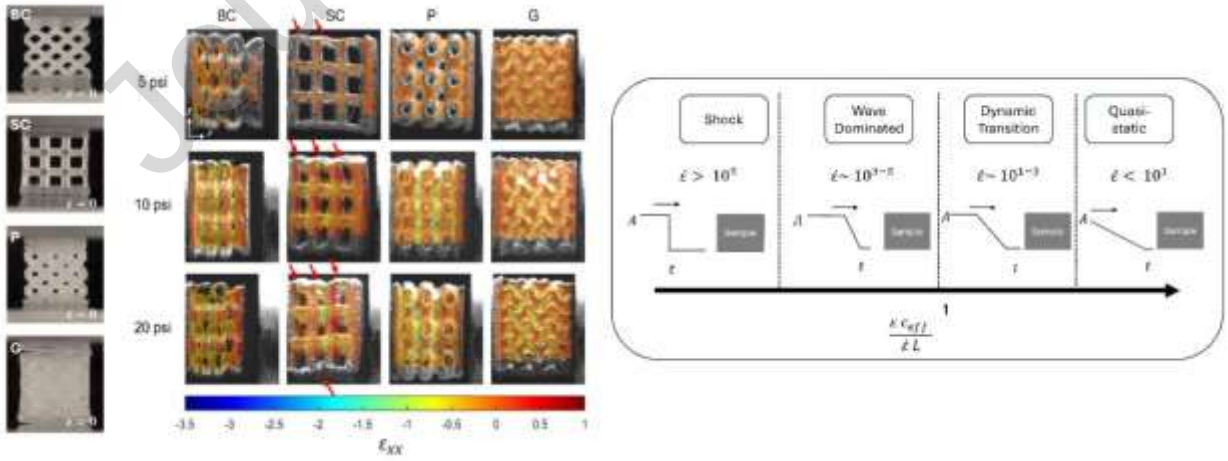

Keywords
Architected materials, strain rate, elastomers, split-Hopkinson pressure bar

1. Introduction

Architected materials (also often referred to as "lattice" materials) have garnered significant interest [1] due to properties such as their high relative stiffness at low weight [2-5], as well as the promise they show in energy absorption applications [2, 3, 6-20]. In recent years, improvements in additive manufacturing (AM) [21] methods have increasingly enabled a high degree of multi-scale tailorability in the structure of such materials. This has expanded researchers' capacity to design the effective properties of such materials, through control of topology and structure. Regarding impact response, for example, by controlling buckling phenomena through 2-D and 3-D ligament and node geometries in polymers, structures have been realized with controlled layer compaction or folding mechanisms under load [2, 7, 8, 10, 18, 22-24]. Other works have explored the effects of negative Poisson ratio during impact [8, 12, 14, 25, 26]. Further, multiple studies have explored how energy absorption varies with constituent material properties [5], relative density [27, 28], strut and wall thickness [29, 30], grading [31, 32], loading direction [21, 33], as well as different types of lattice geometries [29, 34, 35].

The response of architected materials in the low-to-intermediate (up to ~10^4 s^{-1}) strain rate range has been of particular interest due to envisioned uses such as lightweight structural components in automotive and aerospace applications, or blast and shock mitigating materials for soldier, vehicular, and building protection. This range can be thought of as a transition region where there is a potential for the behavior of the architected material to exhibit rate dependency, but the loading has not yet reached the very high strain rates where effects such as structure-independent compaction fully dominate the response. This rate dependency can be expected to manifest in two principal ways, namely constituent material rate dependency and inertial effects at higher strain rates. The onset and qualitative contribution of inertial effects to an architected material object's dynamic response can be expected to depend on the relative characteristic length and time scales of the loading, confinement, material architecture, and the overall object. The effect of strain rate in this regime on the dynamic behavior of architected materials has been studied in a variety of structures, including disordered structures such as foams, honeycombs, triply periodic minimal surface (TPMS) structures, ordered lattices, and lattices with modified struts [10, 23, 31, 36]. The bulk of these dynamic studies, however, have focused on metallic architected materials, rather than polymer ones or, even rarer, soft elastomeric ones. We note that many metallic lattice studies suggest constituent material strain rate dependency, with some explicitly suggesting negligible inertial effects [27, 34, 37]. Others, in contrast, report distinct inertia-induced strain rate sensitivity [38] and velocity-dependent collapse modes [35, 38, 39]. While recognizing the observations for metallic lattices, it is important to note that architected materials made of soft elastomers exhibit significant qualitative differences, including hyperelasticity allowing large strains and viscoelastic effects. Determining the loading conditions at which strain rate begins to dominate, and the associated deformation mechanisms involved as strain rate increases, is important for predicting intermediate-to-high strain rate performance of elastomeric architected materials and designing for enhanced performance in such regimes.

In this work, we explore the <10^3 s^{-1} strain-rate response of four elastomeric architected materials (shown in Fig. 1), wherein we expect both inertial and constituent material strain rate dependence effects may play an important role. Indeed, aside from the previously described strain rate effects observed in architected materials, the soft polymeric materials we study

herein have also been shown to exhibit significant strain rate effects in this regime in bulk form [40]. Using a Split Hopkinson Pressure Bar (SHPB) [41] and a high speed camera paired with digital image correlation [42] [42] techniques, we demonstrate a range of behaviors that dominate the response of AM structures at varying strain rates. From the DIC data, we extract strain fields as a function of time for the dynamically-tested lattices, allowing us to track differences in deformation modes as a function of strain rate. We highlight the effect of both the constituent material properties and the length scales in determining when the transition to strain rate importance occurs, as well as the influence of the lattice geometry in the emergence of distinct deformation modes. We further offer design principles for optimizing responses at differing strain rates, based on the design aspects which determine the dominant deformation mechanisms.

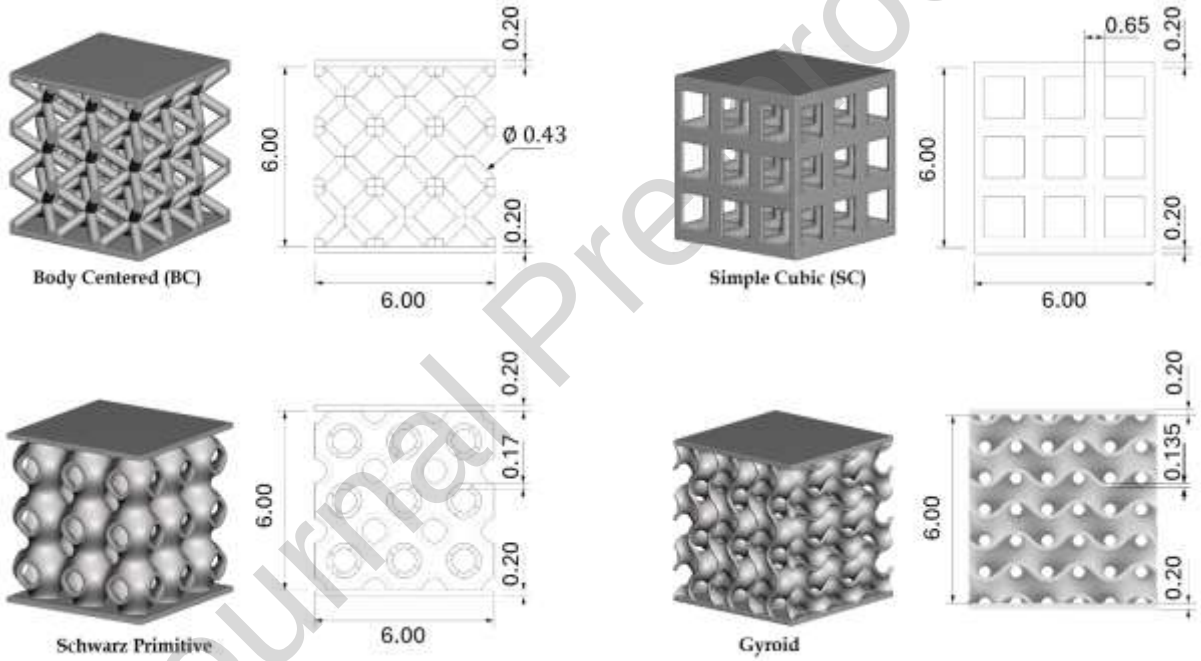

Figure 1. 3D models of four additively-manufactured lattice structures (clockwise from top left) Body Centered (BC), Simple Cubic (SC), Schwarz Primitive (P), and Gyroid (G). All dimensions pictured are in units of mm.

2. Experimental

2.1 Materials and manufacturing methods

Stereolithography (SLA) is an AM process that uses a UV light source to cure resin in a rastering fashion to achieve the final desired 3D topology [43-46]. By adopting SLA technology, lattice structures were printed using Elastic 50A resin (Formlabs Inc.) [47], a photopolymer resin classified as an elastomeric material, on a Formlabs Form3+ instrument. Default printing parameters were controlled by Preform software version 3.24.2. The layer thickness was set to 80 μm, and 0.2 mm of bulk support plate was printed on both the top and

bottom. The printed structures were washed for 3 days in isopropyl alcohol then dried for an additional three days at 40 °C. They were then cured under UV light for 10 min at 40 °C. The solid density of the cured resin was ρ_0 = 1.071 g/cm^3. Four different structures were prepared: simple cubic (SC), body-centered (BC), Schwarz primitive (P), and gyroid (G). The STL files for the structures are shown in Fig. 1. The theoretical (target) strut thicknesses in the print were: SC 650 µm; BC 430 µm; G 135 µm; and P 175 µm. Details about the sample dimensions and densities are given in Table 1.

Table 1. Dimensional details of the four additively-manufactured lattice structures studied herein.

Structure	*Outer dimensions (mm)*		*Strut thickness (*µm*)*			*Structure density (g/cm^3)*	*Effective elasticity modulus (kPa)*
	Theor.[a]	*Exp.*[b]	*Theor.*	*Exp.*[b]	*Difference (%)*		
BC	6x6x6.4	5.6x5.6x5.4	430	459	6.7	0.472	84
SC	6x6x6.4	5.7x5.6x5.5	650	628	3.4	0.456	195
P	6x6x6.4	5.7x5.5x5.4	175	201	14.9	0.561	217
G	6x6x6.4	5.6x5.4x5.3	135	181	34.1	0.718	410

[a] *Including 200 µm plate on the top and bottom.* [b]*Exp. is the average value after three measurements.*

2.2 Quasi-static compression tests

Quasi-static compression measurements were performed on samples of the same type as those outlined in Table 1 using via load frame testing. We note that a separate set of samples was used for quasi-static and dynamic testing. Three tests were performed at $\dot{\varepsilon}$ = 0.2 mm/s to maximum stresses of 0.2 MPa.

2.3 Hopkinson-bar testing

Split-Hopkinson Pressure Bar testing was performed at Los Alamos National Laboratory using an apparatus described previously [41]. Strain gauges (Dynasen, Inc.) were glued on the incident bar and transmission bar. Three firing pressures (5 psi, 10 psi, and 20 psi) were used to launch the incident bar at velocities of ~32.7 m/s, ~47.6 m/s, and ~62.5 m/s. Each sample had a speckle pattern applied to the surface, using spray paint, prior to testing. A Shimadzu HPV-X high speed camera (500,000 frames per second) was used to capture video of the SHPB tests, allowing for the use of digital image correlation[48][49] methods. Due to weak transmitted signals typical of elastomers, we focus on the DIC data obtained from these experiments and use the SHPB as a loading mechanism only.

3. Results

3.1 Quasi-static compression

Under the low strain-rate compression, the four AM structures exhibited different mechanical responses owing to the deformation and compaction mechanisms associated with their respective topologies. The resulting stress-strain curves are shown in Fig. 2. Optical images at several points throughout the compression test for each structure are shown in Fig. 3. Each sample was subjected to four consecutive loading cycles. A linear fit to the elastic region (up to $\epsilon \approx 10\%$, see SI for fits) of the first cycle stress-strain curve was used to calculate the effective elastic modulus for the structure. These values are recorded in Table 1.

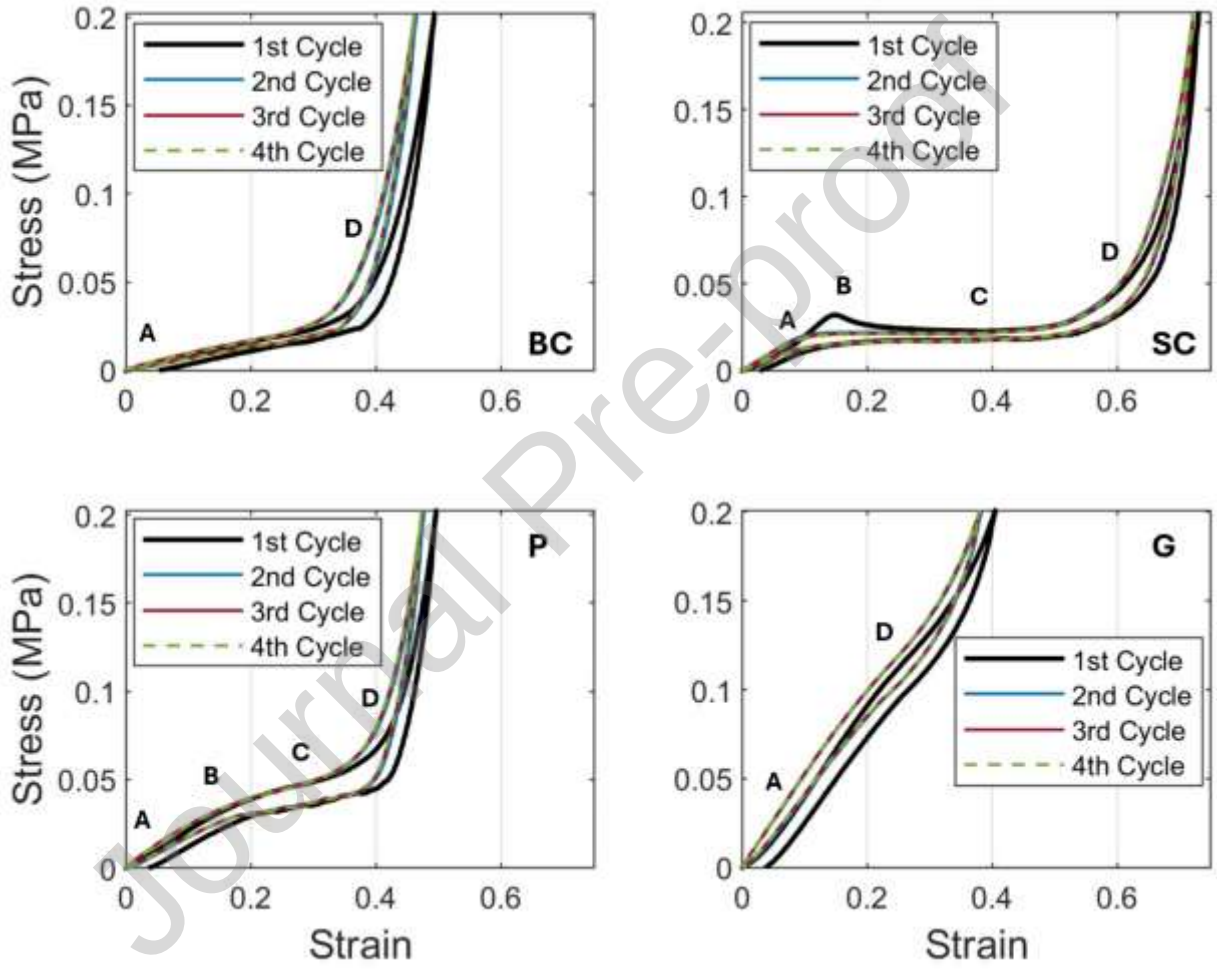

Figure 2. Stress-strain curves from quasi-static compression experiments to a maximum stress of 0.2 MPa. Clockwise from top left: BC, SC, P, and G structures, are as described in the Experimental Section and shown in Fig. 1. We note that the 2nd, 3rd, and 4th loading cycles are very similar, and overlay one another on the plots. The curves are annotated to describe regions of deformation behaviors: A) Quasi-elastic loading, B) Structural Yield, C) Plateau, and D) Significant structure self-contact and densification. Stress-strain curves for two additional maximum stress test values are given in the Supplementary Information.

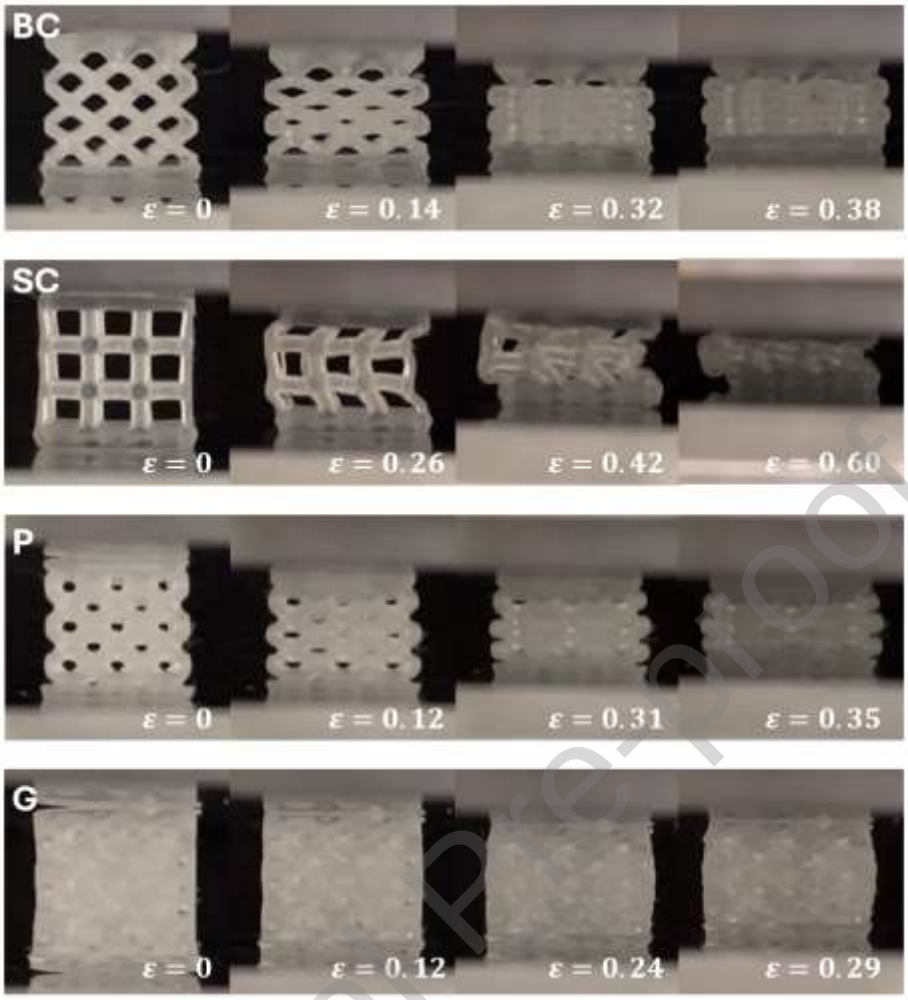

Figure 3. Optical images of the BC, SC, P, and G structures (top to bottom), taken during the quasi-static compression tests shown in Fig. 2.

For the BC structure a relatively linear stress vs. strain (σ vs. ϵ) response can be seen until $\epsilon \approx 30\%$. This effective modulus is relatively soft compared to the other lattices, as expected as it is a "bend dominated" lattice (referring to its connectivity being less than the Maxwell criterion) [50]. The "accordion-like" mode of deformation for this strain region can be seen in the first two panels of the top row of Fig. 3. The influence of this initial mode of deformation makes distinguishing distinct regions of structural yield and plateau behavior from the quasi-elastic behavior nontrivial, and we therefore leave the entire region labeled as quasi-elastic in Fig. 2A. At $\epsilon > 30\%$, we see a progressive densification of the lattice, shown in the third panel of the same row in Fig. 3, and by the significantly increased effective modulus in this strain region in Fig. 2a (reaching full densification at $\epsilon \approx 35\%$). Upon unloading, a small hysteresis can be observed, which may be related to either viscoelastic or plastic deformation processes. Subsequent loading cycles show roughly similar low strain behavior, but a slightly lowered densification strain.

We next consider the SC structure in Fig. 2b, with the corresponding deformation images in the second row of Fig. 3. The SC structure displayed structural instability at $\epsilon \approx 20\%$ resulting in buckling of the lattice elements aligned with the compression axis. The initial, pre-buckling effective modulus of the lattice can be seen to be significantly higher than the BC

lattice, dropping to a near-zero modulus plateau. We draw attention to the brief region of negative stiffness during the initial loading cycle (black line), which is a result of the buckling observed in the lattice. This negative stiffness region is of particular note in that it is behavior associated with a 'Type II' structure (defined by a region of decreasing force in the force-displacement curve), which has been shown to have implications for the rate sensitivity of a lattice.[51] Further loading past the plateau resulted in a continuation of the plateau until progressive densification, denoted by the rapid rise in stress at $\epsilon \approx 50\%$ to 60% strain. In contrast to the BC lattice, a qualitative behavior change can be seen after the first loading cycle, where the clear peak in stress around $\epsilon \approx 15\%$ disappears, which suggests the presence of at least some local irreversible process (either plasticity or fracture), although the total permanent strain retained after unloading is still minimal

The P structure at first displayed a nearly linear behavior of similar stiffness to the SC lattice (*i.e*. stiffer than the BC structure). As seen in Fig. 2c and the first two images in the third row of Fig. 3, it began to exhibit softening behavior around $\epsilon \approx 20\%$ as the voids changed shape and began to collapse. Significant densification begins to occur in the $\epsilon \approx 30\%$ to 40% range (right two images in the third row of Fig. 3), marked by a shift to stiffening behavior, quickly followed by a sharp rise in stress in the $\epsilon > 40\%$ region. Similar to the BC structure, in subsequent loading cycles we observe very similar behavior at lower strains, but a slightly lowered densification strain (closer to the lower end of the $\epsilon \approx 30\%$ to 40% range).

The high initial density (low porosity) of the G lattice (see Table 1) resulted in earlier (relative to the other structures) ligament contact and densification, leading to much stiffer initial behavior, as seen in Fig. 2d. The structure can be seen to maintain a quasi-linear behavior until $\epsilon \approx 20\%$ (left two images of the bottom row of Fig. 3), followed by a period of weak softening until $\epsilon \approx 30\%$. This softening region is accompanied by a bulging outward of the sides of the structure, as seen in the right two images of the bottom row of Fig. 3. This slight softening is followed by a shift back to stiffening at $\epsilon > 30\%$. Subsequent loading cycles result in a shift to the left of the entire curve, again suggesting irreversible processes.

The specific energy absorption [52] of each lattice, taken as the area under the initial load-displacement curve divided by the mass of the structure, is calculated to be 58.16 J/kg (SC), to 50.58J/kg (G), to 44.59 J/kg (P), to 36.76 J/kg (BC). The ability of the SC structure to accommodate large strains via structural yielding gives it the highest quasi-static specific energy absorption.

3.2 Split Hopkinson-bar experiments

For the previously-described SHPB experiments, DIC analysis was performed on the recorded video using the program VIC-2D (Correlated Solutions) (see the SI for more details). Strain fields and displacements were obtained through this analysis, and further processed in MATLAB. Snapshots of the deformed samples at the time of maximum compression are shown in Fig. 4, along with the overlaid strain field in the x direction (ε_{xx}) obtained from DIC (noting the loading is in the x-direction). The impactor is incident from right to left. The transmission bar on the left acts nearly as a rigid boundary due to the limited energy transmitted. It can be seen that increasing the input pressures results in successive increases in global compression (top to bottom rows). This, along with the corresponding increasing strain rate, results in the

activation of different deformation mechanisms and different regions of the stress-strain curves as a function of both lattice type and strain rate.

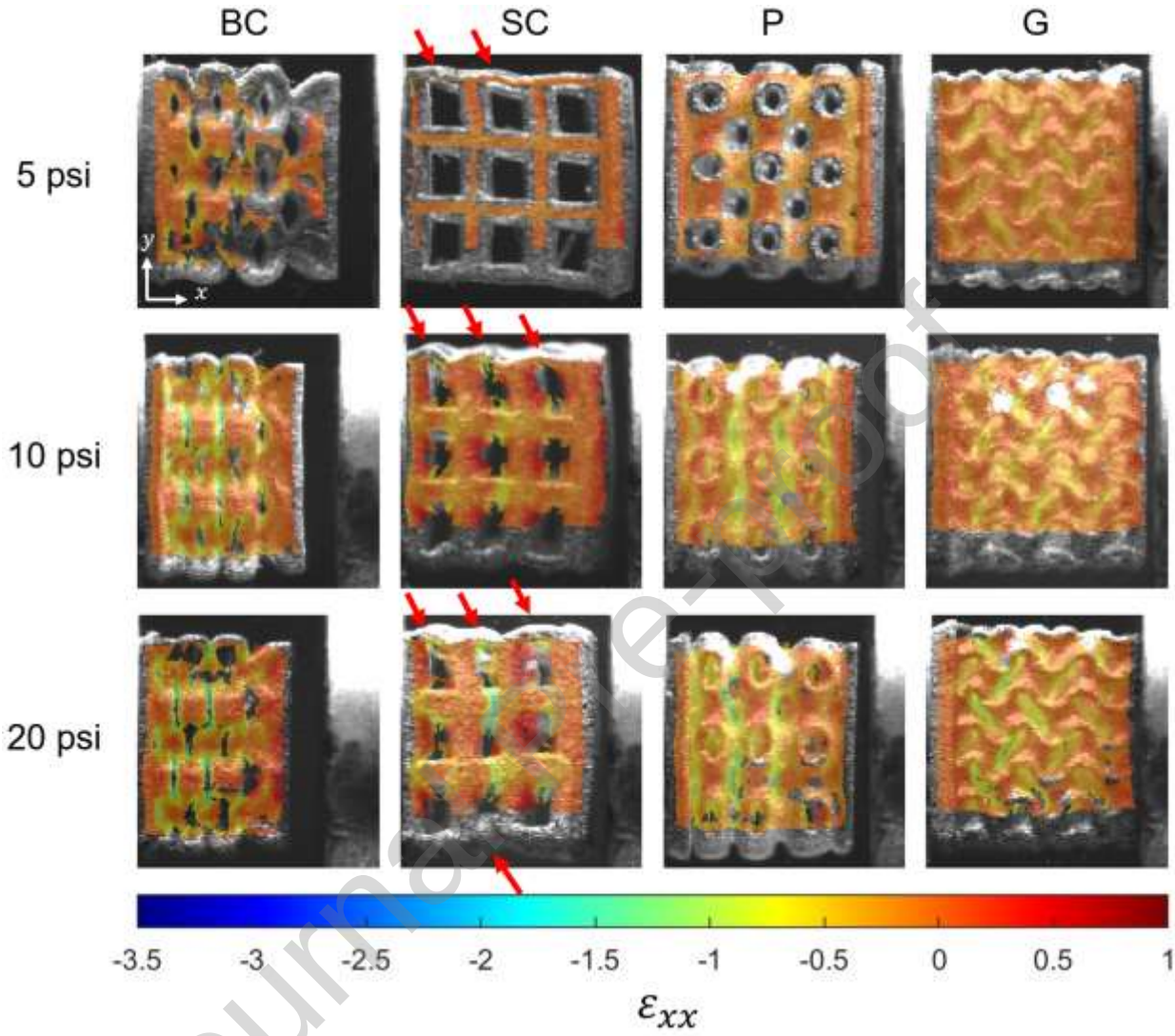

Figure 4. Still images of deformed lattice samples from 12 different tests at the time of maximum compression, with the DIC-calculated *x*-direction strain field (ε_{xx}) layered on top. The tests pictured are of BC, SC, P, and G lattices (left to right columns), and 5 psi, 10 psi, and 20 psi of input pressure (top to bottom), corresponding to ~1500, 2300, and 2800 s^{-1} strain rates, respectively. Red arrows highlight localized buckling.

In Fig. 4, the BC lattice, all strain rates show a smooth collapse of local features from the right to the left, which is indicative of wave-like behavior. As the strain is increased to 2500 s^{-1} and 3000 s^{-1} (middle and bottom rows), self-contact is made between local features (shown in the bottom two BC rows in Fig. 4), engaging the region of densification (the region marked D on the quasi-static curves shown in Fig. 2).

For the SC lattice, we observe at all tested strain rates that deformation of the voids begins with localization at the right edge (close to the impactor) that propagates to the left edge (See videos in SI). At ~1500 s^{-1} (top), we note the onset of localized strut buckling/collapse at the left (next to the transmission bar), as indicated by the red arrows in the second column of

Fig. 4. This could be indicative of dynamic buckling, given the observed initial localized deformation on the right, and may be consistent with stress doubling that occurs at a rigid boundary during wave propagation, wherein the threshold for local buckling may not be reached during the initial transit of the dynamic stimuli across the material. However, this may also be indicative of a more, global, quasi-static buckling process due to a heterogeneous strain field, wherein the initial buckling of one location relieves stress elsewhere. No uniform or long-wavelength global buckling was seen, in contrast to the quasi-static compression tests (e.g. the second panel from the left for the SC lattice in Fig. 2). As the rate is increased further to ~2300 s^{-1} and ~2800 s^{-1} we observe more localized strut buckling (denoted by the red arrows), some of which is out of the 2D camera plane (highlighted by the bottom red arrow in the second column of Fig. 4, and more easily visible in the videos included in the SI). We suggest that the distribution of the localized buckling without apparent self-contact suggests a dynamic buckling process is occurring.

The P and G lattices both exhibit localized deformation of their features which begins concentrated at the right edge and propagates left, eventually settling to a quasi-even distribution across the sample. A change in pore shape is observable in the P lattice, at the two higher strain rates tested, which is consistent with the quasi-static tests and the measured strain fields.

4. Discussion

In this study, we directly compare the deformation mechanisms of several common lattice topologies engaged at strain rates on the order of ~10^3 s^{-1}, with their responses under quasi-static compression. We are interested in studying if, where, and why a 'transition' region might occur, in which the deformation mechanisms shift from those observed in low strain-rate regimes to those in high strain rates regimes. Such details then may be translatable to qualitative design principles for application of hierarchical materials in dynamic loading regimes.

We note that there are two distinct effects that depend upon strain rate which could influence the behavior of the lattice. The first, the strain rate sensitivity of the constituent material, is straightforward, and is influenced principally by the choice of the constituent material and its strain rate-dependent properties. This includes effects such as viscoelasticity or thermal softening, and has been observed in many dynamic lattice investigations [23]. For the material in this work we expect that, due to the damping coefficient ($\tan \delta$) for this class of elastomer being expected to be on the order of ~10^{-1} [53], that at the strain rates tested herein there will be some dynamic, viscoelasticity-driven stiffening [40].This effect may interplay with the architected material's structural geometry, wherein strain localization can lead to locally greater strain rates and thus locally even greater viscoelastic effects. The second effect is the influence of inertia (both micro- and macro-) in the deformation of the geometry [23, 38, 54-58]. The onset of inertial effects also depends not only upon the behavior of the material, but also upon the geometry. We consider that inertial effects tend to take prominence when a 'wave dominated' regime is entered, which we define as occurring approximately when the distance the wave has traveled (effective pulse length) is less than some characteristic structural length scale. Outside of this regime, equilibrium is reached across the length of the sample

during loading without any dynamic localization. The onset of the wave dominated regime can be described by the equation

$$\lambda < L, \tag{1}$$

in which λ is the effective pulse length and L is the characteristic structural length scale. If we take strain rate to be

$$\dot{\varepsilon} = \frac{\delta}{Lt}, \tag{2}$$

where δ is the displacement of the striker bar at some time t, then the condition for wave localization to arise can be written as

$$\frac{c\varepsilon}{\dot{\varepsilon} L} < 1, \tag{3}$$

assuming $\lambda=ct$, $c = \sqrt{E/\rho}$ is the effective speed of sound in the material, in which E is the effective elastic modulus and ρ the effective density of the lattice (values can be found in Table 1). We henceforth refer to the nondimensional quantity $\frac{c\varepsilon}{\dot{\varepsilon} L}$ as the localization parameter, l. Because of the use of the effective speed, c, l incorporates not only constituent material effects, but also structural effects arising from the geometry of the lattice. Length L can be taken to be the length of the undeformed lattice, in which case localization should induce the onset of inertial effects globally, but the structure can still be approximated as a continuum. Alternatively, L can be taken as the unit cell length scale, in which case continuum approximations break down and inertial effects within the unit cell gain importance. This length scale influence is similar to the higher strain rate length-scale-dependent rarefaction wave interactions seen by Dattelbaum et al. [59] in polymer fractal structures under shock loading, as well as considerations noted by Liu et al. [38] regarding metallic cellular foams. The parameter l can aid in judging if a given lattice of a given material can be expected to experience inertial effects arising from wave-driven behavior at a given strain rate. We note, for example, that many of the experiments in literature which report not seeing inertial effects at strain rates similar to those tested herein [27, 33, 36] investigated metallic lattices, which have a much higher effective speed of sound than the soft elastomeric lattices tested herein. This would result in a higher value of l, and therefore under similar loading conditions, we would expect wave effects to gain importance at lower strain rates in the lattices tested here than in similar metallic lattices.

The normal strain fields along the direction of loading (ε_{xx}) are one metric by which wave localization can be examined experimentally. Periodic strain across the length of the sample, commensurate with the unit cell period, would be generally expected when not in a wave-dominated regime [23, 38]. The exception to this would be the presence of mechanical instability, which may cause stochastic, localized sequential buckling [60]. Alternatively, when the loading induces a wave dominated regime, we expect increasingly non-uniform global

strain, concentrated at one edge and moving in the direction of the loading pulse, from which inertia-driven modification of the lattice behavior may arise.

To more easily compare ε_{xx}, the strain field was summed vertically over the width of the sample (transverse to the loading direction), allowing for visualization as a line representative of the strain experienced in the effective material as a function of *x*-dimension, as shown in Fig. 5. In the case of the SC lattice, which has relatively large voids that introduce some noise to the DIC values, strain values overlapping the edges of the voids were removed to smooth the data. This data was then plotted for each experiment to examine the ways in which localization and deformation mechanisms shift as a function of topology and strain rate. Figure 5 shows the early time steps for the 5 psi input pressure cases. The other test cases and times can be found in the SI. As seen in Fig. 5, early time steps clearly show an initial localization of strain on the right (impacted) edge, which then propagates to the left across the sample as the pulse travels across the sample. This non-uniform strain is a clear indication that a wave-dominated regime has emerged, even at the lowest strain rate tested (~1500 s^{-1}).

We estimate the localization parameter *l* for the tested cases, which are listed in Table 2 and plotted in Fig. 6. The localization parameter estimates indicate that all cases tested herein are well within the wave dominated regime, with the highest localization upper limit being on the order of ~0.16, well below unity. For comparison, if the modulus *E* and density ρ were scaled to the range of metals (respectively, 68 GPa and 2.7 g/cm^3 for aluminum, for example), and the same structures, strains, and strain rates were considered, the same estimates would put the localization parameter in the range of 10 – 20 (also plotted in Fig. 6). In addition to the effect of the material, we can see the effect of the structure on the effective speed of sound. The G structure, for example, is the densest and stiffest of the samples tested. While these could be expected to increase proportionally, resulting in the same effective sound speed, the comparatively greater estimated sound speed of the G lattice is consistent with the known loss of relative stiffness in low density lattice materials [4, 19, 61]. In the strain data shown in Fig. 5, the pulse in the G structure can be seen to reach the left edge of the sample faster than the pulses in the other structures. Because of this, although the G structure is still in the wave-dominated regime, the BC, SC, and P structures are more firmly in this regime (lower localization parameter values) due to the structure leading to a shorter effective wavelength.

Figure 5. The time evolution of normal strain in the x direction (material-tied reference frame), summed vertically over the height of the sample, in which the color shift from red to blue

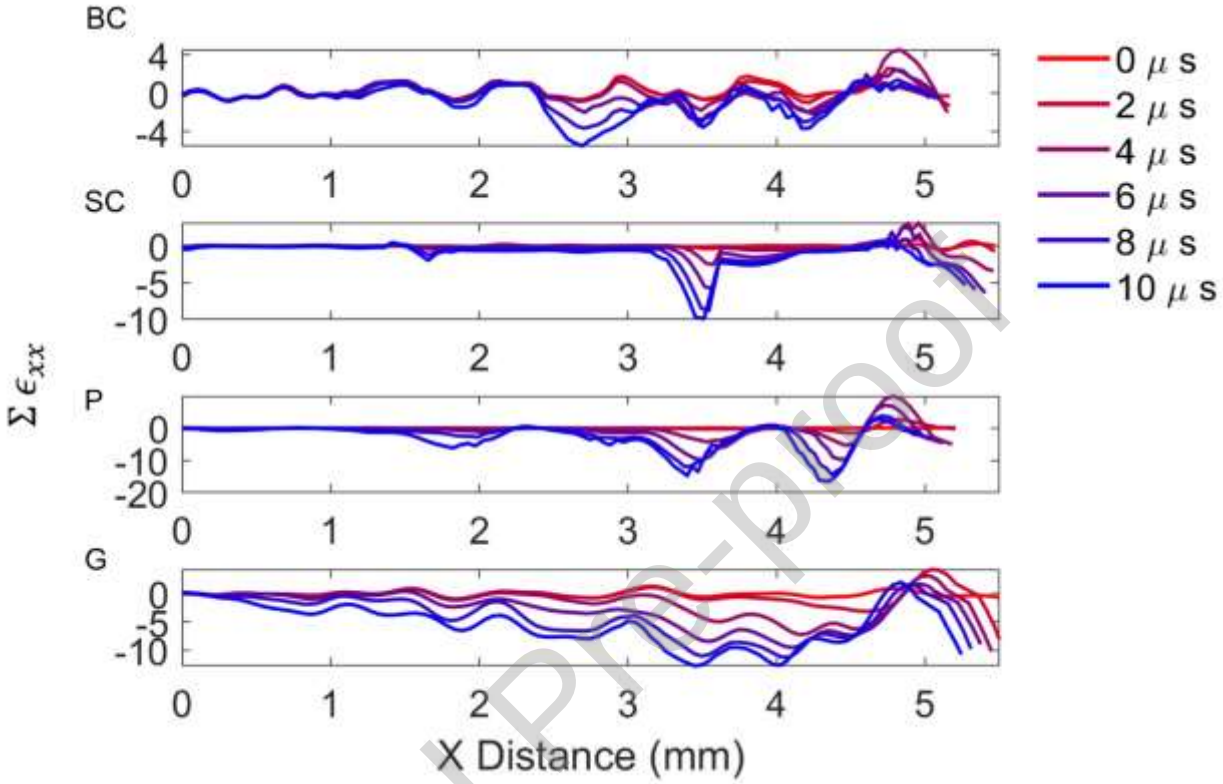

indicates advancing time. Data shown are for the first five frames from impact (0 – 8 μs, as outlined in legend) for A) BC lattice tested at 5 psi, B) SC lattice tested at 5 psi, C) P lattice tested at 5 psi, and D) G lattice tested at 5 psi. The same data for other test pressures, as well as the time evolution for all cases, can be found in the SI.

Table 2. Magnitude and duration of impulse, associated strain rates, and localization estimates from SHPB experiments on the 4 structures.

Sample	Pulse magnitude	Pulse durations	Strain rates	Max	Estimated	Estimated upper

	ε (5 psi, 10 psi, 20 psi)	(μs) (5 psi, 10 psi, 20 psi)	(s^{-1}) (5 psi, 10 psi, 20 psi)	average $d\varepsilon_{xx}/dx$ (5 psi, 10 psi, 20 psi)	upper limit c (m/s)	limit $\frac{c\varepsilon}{\dot{\epsilon} L}$ (5 psi, 10 psi, 20 psi)
BC	0.06, 0.10, 0.12	0.52, 0.53, 0.55	1500, 2500, 3000	0.055, 0.182, 0.203	13.1	0.088, 0.090, 0.095
SC	0.06, 0.09, 0.11	0.53, 0.52, 0.56	1500, 2300, 2800	0.023, 0.096, 0.153	19.1	0.131, 0.134, 0.139
P	0.06, 0.09, 0.11	0.52, 0.52, 0.55	1500, 2200, 2800	0.046, 0.089, 0.105	19.2	0.123, 0.125, 0.134
G	0.06, 0.08, 0.11	0.52, 0.53, 0.55	1500, 2100, 2800	0.032, 0.049, 0.067	25.4	0.160, 0.153, 0.156

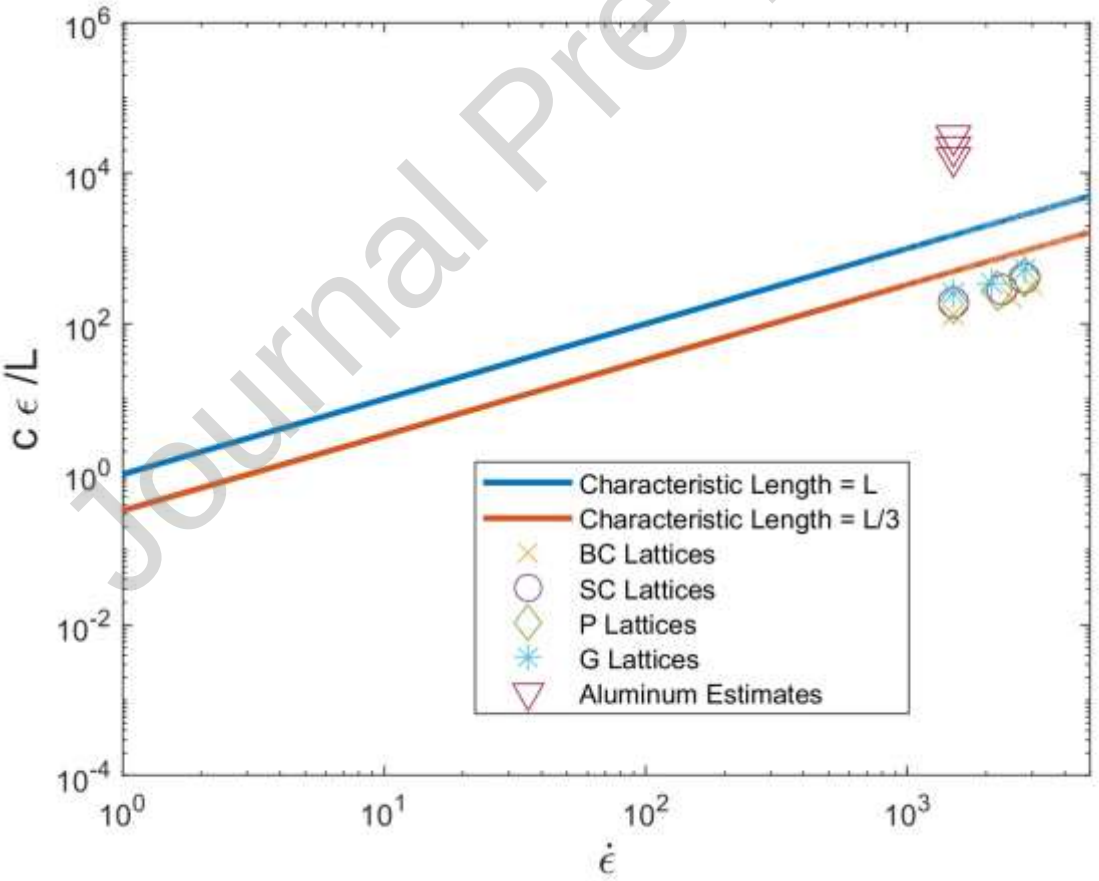

Figure 6: Three variables of the localization parameter plotted against strain rate. Solid lines represent the threshold across which wave localization occurs for differing characteristic lengths, with the data points from this work additionally highlighted.

With regard to the mode of deformation, one of the most notable differences between the quasi-static and dynamic tests is the appearance of dynamic inertial stabilization in the SC lattice. Under quasi-static compression, a global, long wavelength, asymmetric buckling mode becomes energetically favorable at low strains (see Figs. 2 and 3). When dynamically compressed, particularly at the higher strain rates, we see a shorter wavelength, periodic, and globally axially symmetric, buckling mode appear. These local modes are triggered despite the tendency for the global buckling mode to be more energetically favorable, due to the shorter pulse length (*i.e.* wave dominated localization) present in the dynamic loading scenario – a well-known phenomenon in the study of dynamically buckling beams [62, 63]. It is worth noting that this dynamic buckling has implications for the impact mitigation performance of the structure, as dynamic buckling has been shown to stabilize buckling, delaying its onset and allowing for the support of greater axial loads up to higher displacements than would occur quasi-statically [62, 63]. Indeed, lateral inertia of the buckling elements has previously been shown to play a role in strain rate sensitivity [4, 38, 51, 64]. The higher two dynamic strain rates tested, and potentially the lower strain rate tested, demonstrated inertial stabilization and localized dynamic buckling for the SC lattice, further highlighting the onset of a regime in which inertial effects have begun to gain importance.

To explore the differences in deformation modes and localization as a function of geometry, the gradients of the ε_{xx} strain fields were examined. Gradients were taken with respect to the deformed x-coordinates (material-tied reference frame), smoothed, and the absolute value was taken to avoid positive and negative strains canceling out. Gradients were then averaged over the entire sample for each time (see SI). The maximum averaged gradient values from each test are summarized in Table 2 and plotted in Fig. 7, in which it can be seen that, as expected, strain localization increases as maximum overall compressive strain increases (noting also that, in the tests herein, increased strain rate correlates with increased maximum compression). If we examine the slopes of the strain gradient trends in Fig. 7, the SC, and to a lesser degree the G, lattice exhibit an increase in localization slope the middle to the highest strain (see SI and Table 2). In the SC lattice, we suggest that this may be due to the dynamic buckling of the struts aligned with the compression direction, wherein the buckling occurs at the unit-cell-scale or below, instead of the sample scale (as in Fig. 2).

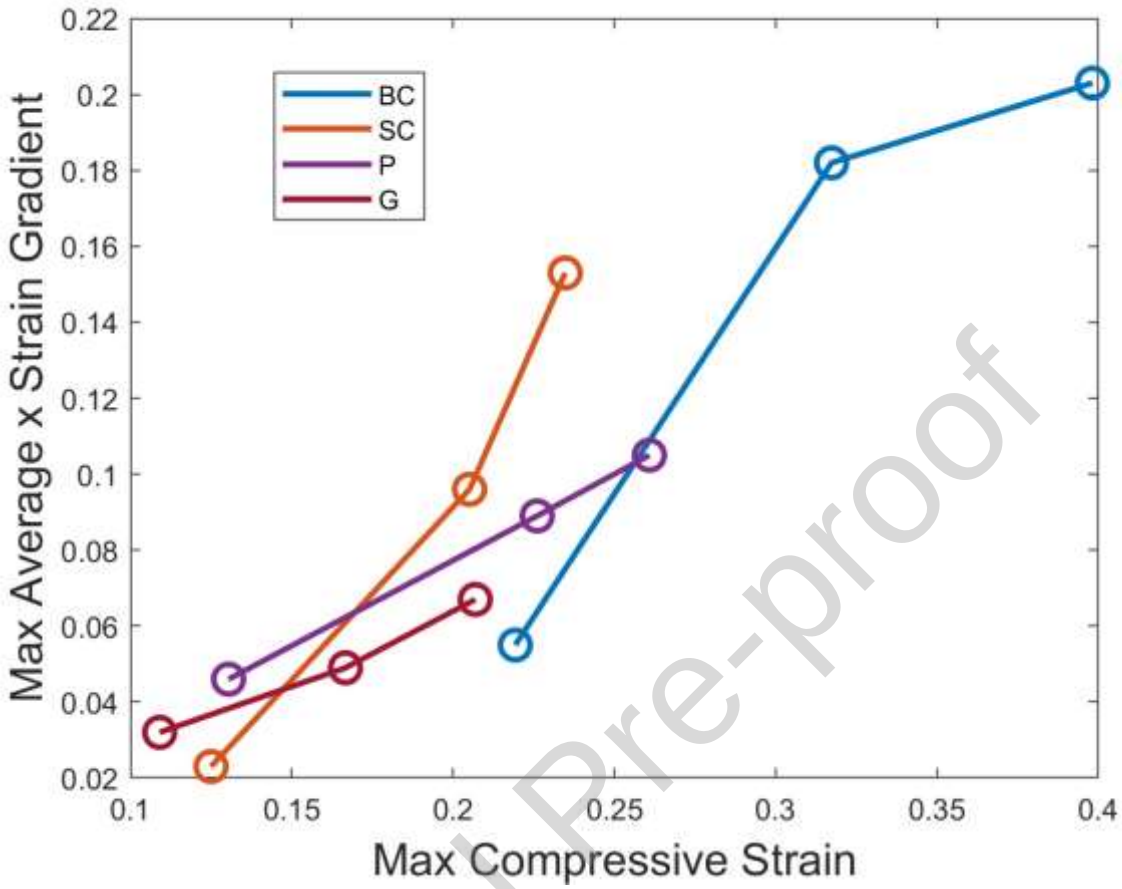

Figure 7: The maximum value of the average strain field gradient ($d\varepsilon_{xx}/dx$) as a function of maximum compressive strain. Note that maximum compressive strain increased with strain rate in these tests.

In the context of examining the effects of geometry upon not only the energy absorption capabilities and deformation mode, but also the strain rate sensitivity, of a structure, we highlight that the deformation behavior of the SC lattice shows marked differences from the other three lattices in both its strain rate-dependent deformation and its deformation-localization slope. We suggest that these differences arise in large part due to the SC lattice being a 'Type II' geometry, as noted in section 3.1 above, while the BC, G, and P lattices can be classed as 'Type I' geometries (wherein Type I is defined as a structure which exhibits a flat or smoothly increasing type force displacement curve, while Type II exhibits a drop, or region of negative stiffness, in the force displacement curve) [51]. Type II structures are more sensitive to rate effects and are characterized by a drop in the force displacement curve after an initial peak - behavior which can be seen (albeit weakly) in the initial quasi-static loading cycle of the SC lattice in Fig. 2. This sharp drop arises due to the presence of buckling inducing a brief negative stiffness regime. Although wave localization can be seen in the strain data for all dynamic cases tested herein, in most cases the primary effect is the onset of layers deforming progressively from the site of impact in qualitatively the same manner as they do in the quasi-static case (albeit with some rate sensitive material behavior and relatively small inertia effects

likely present). It is only in the Type II (SC) lattice that we can see this wave localization result in a qualitatively different deformation mechanism within a unit cell.

5. Conclusions

We have explored the mid-strain rate regime of soft polymer structures produced via AM, in the context of examining the shifting of the engaged deformation mechanisms as a function of strain rate and structure. We have shown that even at the lowest dynamic strain rate tested, there are indications in the strain data that a wave dominated regime, in which inertial effects matter, has been reached. This is despite similar studies in architected materials composed of metal that have often found that only constituent material strain effects exist at similar strain rates. We tie this to the effective wavelength in the material, which depends on the effective speed of sound - a parameter which, crucially, relies directly upon both the material and structure in question. This relationship can be expressed as a dimensionless localization parameter, $\frac{c\varepsilon}{\dot{\varepsilon}L}$, which indicates that a wave dominated regime has been entered when it is below unity. This parameter can be used as a judgment of the type of deformation regime a particular structure/material, at a particular loading rate, can be expected to experience, which informs the most important mechanisms to be engaged. We summarize these differing regimes, as a function of $\frac{c\varepsilon}{\dot{\varepsilon}L}$, in Fig. 8.

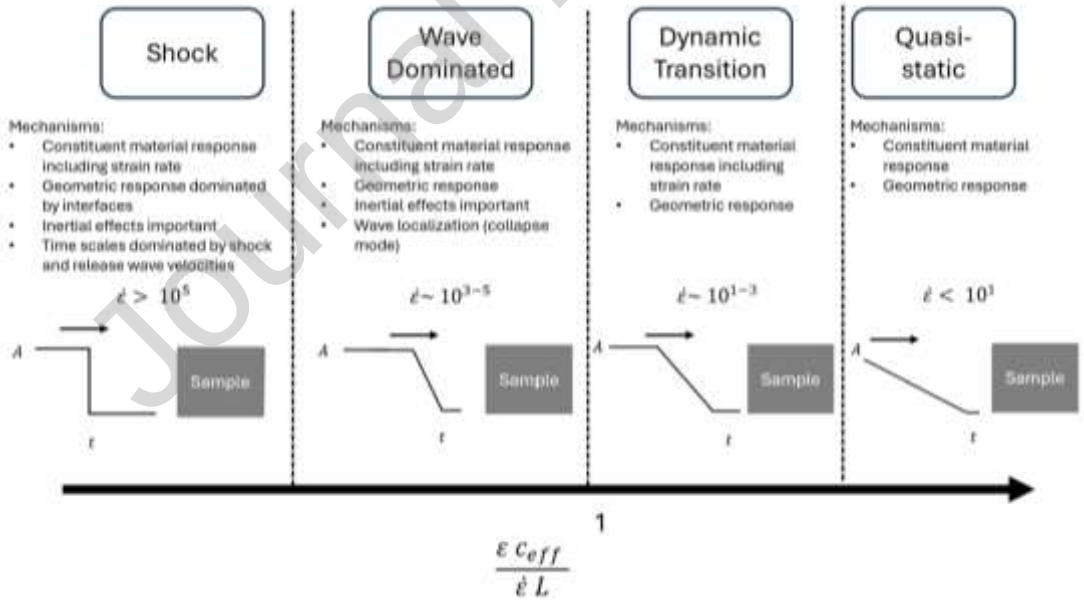

Figure 8: Regime map, outlining the regions in which qualitatively different mechanisms of deformation and energy absorption emerge as a function of the dimensionless parameter described in Equation 3. A shift to a wave dominated regime occurs below a value of 1.

Based upon these insights, we furthermore suggest the following broad design principles for AM lattice structures under dynamic loading. First, that the influence of the constituent material (namely upon ductility, stiffness, and sound speed), structure, and loading

conditions ought to be considered when estimating if a wave dominated regime may be entered. When considering a wave dominated regime, the rate sensitivity of the geometry should be considered important in addition to the rate sensitivity of the constituent material. The type of structure should at this point gain further importance, keeping in mind that Type II structures tend to experience an effective strengthening due to inertial stabilization and dynamic buckling. This dynamic buckling can also be expected to induce a change in the mode of deformation within individual unit cells. Type I structures, meanwhile, may experience successive layer collapse in wave dominated regimes, but are less likely to display intra-cell deformation mode changes. We further suggest that, in making these considerations, it may be helpful to consider the overall strain rate sensitivity as an effective 'material' property, wherein the effective material encompasses both structural and material influences upon the strain rate sensitivity. The localization parameter outlined herein can thus serve as a good rough guide as to expected regime, and therefore the anticipated importance of various mechanisms, which in turn can inform design and tailoring attempts. However, further examination of the space, including higher strain rates and different topologies, would be beneficial in refining estimates and fleshing out the design space.

6. Acknowledgments

This work was supported by the DOE/NNSA Dynamic Materials Properties program. Los Alamos National Laboratory is operated by Triad LLC for the U.S. Department of Energy. B.M. acknowledges support from the U.S. Department of Energy (DOE) National Nuclear Security Administration (NNSA) Laboratory Graduate Residency Fellowship (LRGF) under Cooperative Agreement DE-NA0003960. N.B. acknowledges support from the UC National Laboratory Fees Research Program of the University of California, grant number L22CR4520.

7. References

[1] S. AlMahri, R. Santiago, D.-W. Lee, H. Ramos, H. Alabdouli, M. Alteneiji, Z. Guan, W. Cantwell, M. Alves, Evaluation of the dynamic response of triply periodic minimal surfaces subjected to high strain-rate compression, Additive Manufacturing, 46 (2021).
[2] A.J. Jacobsen, W. Barvosa-Carter, S. Nutt, Compression behavior of micro-scale truss structures formed from self-propagating polymer waveguides, Acta Materialia, 55 (2007) 6724-6733.
[3] T.A. Schaedler, A.J. Jacobsen, W.B. Carter, Materials science. Toward lighter, stiffer materials, Science, 341 (2013) 1181-1182.
[4] S. Lee, F. Barthelat, J.W. Hutchinson, H.D. Espinosa, Dynamic failure of metallic pyramidal truss core materials – Experiments and modeling, International Journal of Plasticity, 22 (2006) 2118-2145.
[5] C. Ling, A. Cernicchi, M.D. Gilchrist, P. Cardiff, Mechanical behaviour of additively-manufactured polymeric octet-truss lattice structures under quasi-static and dynamic compressive loading, Materials & Design, 162 (2019) 106-118.
[6] C. Chadwell, A. Rocco, M. Pankow, The Dynamic Response of Additively Manufactured Polymers Subjected to Tensile Loading, J. Dyn. Behav. Mat., DOI (2022).

[7] T. Cohen, P. Kurzeja, K. Bertoldi, Architected squirt-flow materials for energy dissipation, Journal of the Mechanics and Physics of Solids, 109 (2017) 22-33.
[8] D.M. Correa, e. al., Negative stiffness honeycombs for recoverable shock isolation,, Rapid Prototyping J., 21 (2015) 193-200.
[9] K. Davami, M. Mohsenizadeh, M. Munther, T. Palma, A. Beheshti, K. Momeni, Dynamic energy absorption characteristics of additively-manufactured shape-recovering lattice structures, Mater. Res. Express, 6 (2019) 045302.
[10] E.B. Duoss, e. al., Three-Dimensional Printing of Elastomeric, Cellular Architectures with Negative Stiffness, Adv. Funct. Mater., 24 (2014) 4905-4913.
[11] A.G. Evans, M.Y. He, V.S. Deshpande, J.W. Hutchinson, A.J. Jacobsen, W.B. Carter, Concepts for enhanced energy absorption using hollow micro-lattices, International Journal of Impact Engineering, 37 (2010) 947-959.
[12] N. Fjeldberg, J. Pernas, D. Varas, J. Martin, On the study of the dynamic response in 3D additively manufactured auxetic structures, EPJ Web of Conferences, 250 (2021) 06004.
[13] D.M. Kochmann, K. Bertoldi, Exploiting Microstructural Instabilities in Solids and Structures: From Metamaterials to Structural Transitions, Applied Mechanics Reviews, 69 (2017).
[14] H.M.A. Kolken, A.A. Zadpoor, Auxetic mechanical metamaterials, RSC Adv., 7 (2017) 5111.
[15] S.H. Lee, C.M. Park, Y.M. Seo, Z.G. Wang, C.K. Kim, Acoustic metamaterial with negative modulus, J Phys Condens Matter, 21 (2009) 175704.
[16] J.A. Lewis, Direct Ink Writing of 3D Functional Materials, Advanced Functional Materials, 16 (2006) 2193-2204.
[17] V. Monfared, H.R. Bakhsheshi-Rad, S. Ramakrishna, M. Razzaghi, F. Berto, A Brief Review on Additive Manufacturing of Polymeric Composites and Nanocomposites, Micromachines, 12 (2021) 704.
[18] J.T. Overvelde, S. Shan, K. Bertoldi, Compaction through buckling in 2D periodic, soft and porous structures: effect of pore shape, Adv Mater, 24 (2012) 2337-2342.
[19] T.A. Schaedler, A.J. Jacobsen, A. Torrents, A.E. Sorensen, J. Lian, J.R. Greer, L. Valdevit, W.B. Carter, Ultralight metallic microlattices, Science, 334 (2011) 962-965.
[20] S.J. Talley, B. Branch, C.F. Welch, C.H. Park, J. Watt, L. Kuettner, B. Patterson, D.M. Dattelbaum, K.-S. Lee, Impact of filler composition on mechanical and dynamic response of 3-D printed silicone-based nanocomposite elastomers, Composites Science and Technology, 198 (2020).
[21] B.A. Branch, e. al., Directional shock diode behavior through the interaction of geometric voids in engineered polymer assemblies, J. Appl. Phys., 128 (2021) 245903.
[22] S. Duan, Y. Tao, H. Lei, W. Wen, J. Liang, D. Fang, Enhanced out-of-plane compressive strength and energy absorption of 3D printed square and hexagonal honeycombs with variable-thickness cell edges, Extreme Mechanics Letters, 18 (2018) 9-18.
[23] Y. Sun, Q.M. Li, Dynamic compressive behaviour of cellular materials: A review of phenomenon, mechanism and modelling, International Journal of Impact Engineering, 112 (2018) 74-115.
[24] S. Nakarmi, J. Kim, L.B. Bezek, J.A. Leiding, K.-S. Lee, N.P. Daphalapurkar, The role of unit cell topology in modulating the compaction response of additively manufactured cellular materials using simulations and validation experiments, Modelling and Simulation in Materials Science and Engineering, 32 (2024).
[25] S. Babaee, J. Shim, J.C. Weaver, E.R. Chen, N. Patel, K. Bertoldi, 3D soft metamaterials with negative Poisson's ratio, Adv Mater, 25 (2013) 5044-5049.
[26] Z.G. Nicolaou, A.E. Motter, Mechanical metamaterials with negative compressibility transitions, Nat Mater, 11 (2012) 608-613.

[27] T. Tancogne-Dejean, A.B. Spierings, D. Mohr, Additively-manufactured metallic micro-lattice materials for high specific energy absorption under static and dynamic loading, Acta Materialia, 116 (2016) 14-28.
[28] N. Jin, F. Wang, Y. Wang, B. Zhang, H. Cheng, H. Zhang, Failure and energy absorption characteristics of four lattice structures under dynamic loading, Materials & Design, 169 (2019).
[29] N. Jin, F. Wang, Y. Wang, B. Zhang, H. Cheng, H. Zhang, Failure and energy absorption characteristics of four lattice structures under dynamic loading, Materials & Design, 169 (2019) 107655.
[30] D. Ruan, G. Lu, B. Wang, T.X. Yu, In-plane dynamic crushing of honeycombs—a finite element study, International Journal of Impact Engineering, 28 (2003) 161-182.
[31] B. Branch, A. Ionita, B.E. Clements, D.S. Montgomery, B.J. Jensen, B. Patterson, A. Schmalzer, A. Mueller, D.M. Dattelbaum, Controlling shockwave dynamics using architecture in periodic porous materials, J. Appl. Phys., 121 (2017) 135102.
[32] L. Xiao, W. Song, Additively-manufactured functionally graded Ti-6Al-4V lattice structures with high strength under static and dynamic loading: Experiment, International Journal of Impact Engineering, 111 (2018) 255-272.
[33] J. Mueller, K.H. Matlack, K. Shea, C. Daraio, Energy Absorption Properties of Periodic and Stochastic 3D Lattice Materials, Advanced Theory and Simulations, 2 (2019) 1900081.
[34] S. AlMahri, R. Santiago, D.-W. Lee, H. Ramos, H. Alabdouli, M. Alteneiji, Z. Guan, W. Cantwell, M. Alves, Evaluation of the dynamic response of triply periodic minimal surfaces subjected to high strain-rate compression, Additive Manufacturing, 46 (2021) 102220.
[35] Z. Ozdemir, E. Hernandez-Nava, A. Tyas, J.A. Warren, S.D. Fay, R. Goodall, I. Todd, H. Askes, Energy absorption in lattice structures in dynamics: Experiments, International Journal of Impact Engineering, 89 (2016) 49-61.
[36] J. Lind, A.K. Robinson, M. Kumar, Insight into the coordinated jetting behavior in periodic lattice structures under dynamic compression, Journal of Applied Physics, 128 (2020) 015901.
[37] N. Novak, O. Al-Ketan, L. Krstulović-Opara, R. Rowshan, R.K. Abu Al-Rub, M. Vesenjak, Z. Ren, Quasi-static and dynamic compressive behaviour of sheet TPMS cellular structures, Composite Structures, 266 (2021) 113801.
[38] Y.D. Liu, J.L. Yu, Z.J. Zheng, J.R. Li, A numerical study on the rate sensitivity of cellular metals, International Journal of Solids and Structures, 46 (2009) 3988-3998.
[39] X. Cao, D. Xiao, Y. Li, W. Wen, T. Zhao, Z. Chen, Y. Jiang, D. Fang, Dynamic compressive behavior of a modified additively manufactured rhombic dodecahedron 316L stainless steel lattice structure, Thin-Walled Structures, 148 (2020) 106586.
[40] R. Lakes, Viscoelastic Materials, Cambridge University Press2009.
[41] G.T. Gray, Classic Split-Hopkinson Pressure Bar Testing, in: D.M. Howard Kuhn (Ed.) Mechanical Testing and Evaluation, ASM Handbook, ASM International2000, pp. 462–476.
[42] M. Kadic, T. Bückmann, N. Stenger, M. Thiel, M. Wegener, On the practicability of pentamode mechanical metamaterials, Applied Physics Letters, 100 (2012).
[43] M. Mukhtarkhanov, A. Perveen, D. Talamona, Application of stereolithography based 3D printing technology in investment casting, Micromachines 11:10 (2020) 946.
[44] A. Ramya, S.L. Vanapa, 3D printing technologies in various applications, Journal of Mechanical Engineering and Technology 7:3 (2016) 396-409.
[45] J. Huang, Q. Qin, J. Wang, A review of stereolithography: Processes and systems., Processes 8(2020) 1138.
[46] P. Robles Martinez, A.W. Basit, S. Gaisford, The history, developments and opportunities of stereolithography, 3D Printing of Pharmaceuticals, DOI (2018) 55-79.
[47] Formlabs, Form 3+, 2024, pp. https://formlabs.com/3d-printers/resin/tech-specs/.

[48] B. Pan, Digital image correlation for surface deformation measurement: historical developments, recent advances and future goals, Measurement Science and Technology, 29 (2018).
[49] M.A. Sutton, J.-J. Orteu, H.W. Schreier, mage Correlation for
Shape, Motion and
Deformation Measurements. Basic Concepts, Theory and Applications, Springer2009.
[50] V.S. Deshpande, M.F. Ashby, N.A. Fleck, Foam topology: bending versus stretching dominated architectures, Acta Materialia, 49 (2001) 1034-1040.
[51] C.R. Calladine, R.W. English, Strain-rate and inertia effects in the collapse of two types of energy-absorbing structure, International Journal of Mechanical Sciences, 26 (1984) 689-701.
[52] A. Sarracino, C.I. Hammetter, S.R. Whetten, S.R. Bishop, C.A. McCoy, P.G. Clem, M.B. Sinclair, L.B. Biedermann, M.J. Abere, Elastic wave suppression through additively manufactured petal lattice metamaterials, Journal of Applied Physics, 135 (2024) 165108.
[53] Z.S. Petrović, F. Koco, L. Horvath, N. Dulić, Dielectric properties of segmented polytetramethyleneoxide-based polyurethanes, J. Appl. Poly. Sci., 38 (1989) 1929-1940.
[54] V.S. Deshpande, N.A. Fleck, High strain rate compressive behaviour of aluminium alloy foams, International Journal of Impact Engineering, 24 (2000) 277-298.
[55] X.Y. Su, T.X. Yu, S.R. Reid, Inertia-sensitive impact energy-absorbing structures part I: effects of inertia and elasticity, International Journal of Impact Engineering, 16 (1995) 651-672.
[56] Z. Qin, D. Zheng, X. Li, H. Wang, Influence of Inertia on the Dynamic Compressive Strength of Concrete, Materials (Basel), 15 (2022).
[57] D.E. Grady, Local inertial effects in dynamic fragmentation, Journal of Applied Physics, 53 (1982) 322-325.
[58] P.J. Tan, J.J. Harrigan, S.R. Reid, Inertia effects in uniaxial dynamic compression of a closed cell aluminium alloy foam, Materials Science and Technology, 18 (2013) 480-488.
[59] D.M. Dattelbaum, e. al., Shockwave dissipation by interface-dominated porous structures, AIP Advances, 10 (2020) 075016.
[60] A. Torrents, T.A. Schaedler, A.J. Jacobsen, W.B. Carter, L. Valdevit, Characterization of nickel-based microlattice materials with structural hierarchy from the nanometer to the millimeter scale, Acta Materialia, 60 (2012) 3511-3523.
[61] X. Zheng, H. Lee, T.H. Weisgraber, M. Shusteff, J. DeOtte, E.B. Duoss, J.D. Kuntz, M.M. Biener, Q. Ge, J.A. Jackson, S.O. Kucheyev, N.X. Fang, C.M. Spadaccini, Ultralight, ultrastiff mechanical metamaterials, Science, 344 (2014) 1373-1377.
[62] J.R. Gladden, N.Z. Handzy, A. Belmonte, E. Villermaux, Dynamic Buckling and Fragmentation in Brittle Rods, Phys. Rev. Lett., 94 (2005) 035503.
[63] D.G. Vaughn, J.W. Hutchinson, Bucklewaves, European Journal of Mechanics - A/Solids, 25 (2006) 1-12.
[64] X. Li, M. Ghasri-Khouzani, A.A. Bogno, J. Liu, H. Henein, Z. Chen, A.J. Qureshi, Investigation of Compressive and Tensile Behavior of Stainless Steel/Dissolvable Aluminum Bimetallic Composites by Finite Element Modeling and Digital Image Correlation, Materials (Basel), 14 (2021).

Declaration of interests

☒ The authors declare that they have no known competing financial interests or personal relationships that could have appeared to influence the work reported in this paper.

☐ The authors declare the following financial interests/personal relationships which may be considered as potential competing interests: